

IMU-based online multi-lidar calibration without lidar odometry

Sandipan Das^{1,2}, Bengt Boberg²

When deploying autonomous systems that require several sensors for perception, accurate and reliable extrinsic calibration is required. In this research, we offer a reliable technique that can extrinsically calibrate numerous lidars in the base frame of a moving vehicle without the use of odometry estimation or fiducial markers. Our method is based on comparing the raw IMU signals between a collocated IMU present with the lidar and the IMU measurements from the GNSS system in the vehicle base frame. Additionally, based on our observability criterion, we choose measurements that include the most mutual information rather than comparing all comparable IMU readings. This enables us to locate the measurements that are most useful for real-time calibration. Utilizing data gathered from Scania test vehicles with various sensor setups, we have successfully validated our methodology.

I. INTRODUCTION

For safe navigation and redundancy, autonomous vehicles need numerous sensors to generate 360° sensing coverage. Therefore, it is crucial to establish the precise mounting location for the vehicle's sensors, a process known as extrinsic calibration. Without the proper extrinsic calibration parameters, it is impossible to fuse the sensing data into a single reference frame. We concentrated on multi-lidar system extrinsic calibration in our work. The same principle, though, might also be applied to other modalities.

There are two methods for extrinsic calibration: offline and online. Putting fiducial markers in their shared field-of-view (FoV) of both sensors allows the lidars' characteristics to be matched offline [1], [2]. Online calibration is carried out by comparing the estimated states of the sensor to those in the relevant sensor frame [3], [4], [5], [6], [7]. Since the sensors may not have a common field of view, it is preferable to execute online calibration because it requires less engineering work than an offline method. In online calibration, it is widely recognized that not all motion segments give the information necessary for extrinsic calibration [8], [9], [10]. Hence, identifying the degenerate motion segments helps to discard information that is not necessary for extrinsic calibration computation.

We offer an alternative vehicle-run, an observability-aware online calibration method for simultaneously calibrating multiple lidars using collocated IMU (Inertial measurement unit) signals without the need for state estimation. This method can be extended to other modalities seamlessly and

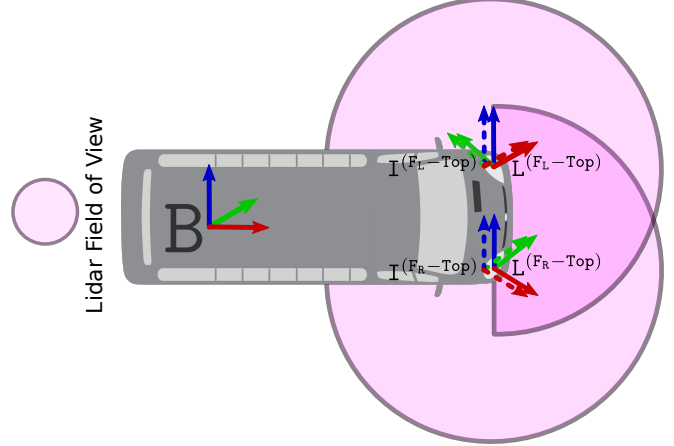


Fig. 1: Illustration of the 2 lidars with their embedded IMUs positioned around one data collection vehicle, when the sensors are calibrated. The vehicle base frame B, is located at the center of the rear axle. The sensor frames of the lidars are: $L^{(F_L-Top)}$ and $L^{(F_R-Top)}$, whereas, the sensor frames of the IMUs are: $I^{(F_L-Top)}$ and $I^{(F_R-Top)}$. (F_L): front-left and (F_R): front-right.

does not require common FoV in between the sensors. Additionally, we compensate for the biases of the IMU measurements online for improving the calibration accuracy.

A. Motivation

As seen in the Fig. 1, the mobile platforms we employed for our studies have a wide variety of sensors. Therefore, it is essential to confirm that the sensors are correctly calibrated prior to any autonomous run. As a result, we must calibrate every sensor online with respect to a common reference frame, which is often found in the middle of the rear axle of the vehicle. The state estimates for motion-based online calibration have intrinsic drifts under aggressive maneuvers which are needed for online calibration to excite the different degrees of freedom. It could therefore cause inaccuracies in the calibration process.

This is why we propose calibrating the lidars using a comparison of the raw IMU signals (with bias compensation) between the collocated IMU(s) with the lidar(s), and the IMU signals from the GNSS system calibrated to the vehicle reference frame. Our approach is based on comparing the raw measurements, as opposed to comparing estimated states, which by their very nature contain process noise. Furthermore, we solely compare the raw angular velocity data for observability analysis.

¹ KTH EECS, Sweden. sandipan@kth.se

² Scania, Sweden. {sandipan.das, bengt.boberg}@scania.com

B. Contribution

The extensive literature on motion-based calibration serves as the inspiration for our work. We would want to contribute the following:

- An observability-aware extrinsic calibration algorithm to calibrate multiple lidars online using collocated IMUs without the need of lidar odometry estimation.
- Online bias compensation of the IMU signals to improve the quality of the extrinsic calibration algorithm.
- Verification of our method based on data collected from Scania autonomous vehicles with the sensor setup shown in Fig. 2, with FoV schematics similar to Fig. 1.

II. RELATED WORK

Extrinsic sensor calibration is a well studied area. In our discussion we briefly review the relevant literature and motivate our choice of method.

A. Offline calibration

Offline extrinsic calibration is performed by matching known markers placed in the common FoV of multiple sensors. To calibrate a multi-lidar system, geometric elements including points, lines, and planes were retrieved and matched in [1], [2].

B. Online calibration

Online extrinsic calibration based on the Hand-Eye method [11], [12], [3] is an extensively studied topic. The term “Hand-Eye” refers to early motion-based calibration research that estimated the motion of the gripper (hand) and the camera (eye) while constricting their poses with a fixed rigid body transformation. Multi-camera extrinsic calibration with the Hand-Eye method has been explored in works like Camodocal [4] and recently extended to multi-lidar extrinsic calibration [13], [6], [14].

Instead of performing Hand-Eye calibration, in Kalibr [8] the authors automatically detected sets of measurements from which they could identify an observable parameter space and then performed a maximum likelihood estimate (MLE) by minimizing the errors between landmark observations and their known correspondences. They also discarded parameter updates for numerically unobservant directions and degenerate scenarios. Kalibr was extended towards MIMU calibration [15] based on matching poses fitted to a B-spline and further constraining with known image landmarks. In MIMC-VINS [16], an efficient multi-state constraint Kalman filter was used to jointly propagate all IMU states while enforcing rigid body constraints between the IMUs during the filter update stage, which produced the MIMU calibration.

We claim that because we have integrated IMUs in our setup, calibrating the multi-IMU (MIMU) configuration will enable us to retrieve extrinsics from the multi-lidar system, given the lidar-IMU extrinsics are known. We also selected measurements that have enough signal excitation known as observability-aware criteria. Nilsson et al. [17] provided housing with noncoplanar orientations for observability analysis, in which their MIMU setup was placed and the



Fig. 2: Reference frames conventions for our vehicle platform. The world frame W is a fixed frame, while the base frame B , as shown in Fig. 1, is located at the rear axle center of the vehicle. Each sensor unit contains the two optical frames C , an IMU frame, I , and lidar frame L .

IMU measurements were matched using MLE. Since we wanted to calibrate the sensors directly in the vehicle, our observability-aware criteria closely resemble work by Jiajun et al. [7]. However, unlike prior work, we maximized mutual information between the angular velocity signals to identify relevant motion segments.

Unlike prior work, we used the fundamental tenet that a rigid body’s angular velocity is constant around every point of the body as the foundation for our MIMU calibration. We used MLE to match the raw angular velocity between the IMU(s) embedded within the lidar(s) and GNSS system and recovered the extrinsics in accordance with the signal-to-signal match principle [18]. We also estimated the IMU biases online by capturing data in a special sequence, removing the need for any exteroceptive modality.

III. PROBLEM STATEMENT

A. Sensor platform and reference frames

The sensor platform with its corresponding reference frames is shown in Fig. 2 along with the illustrative sensor FoV of the bus in Fig. 1. Each of the sensor housings contains a lidar with an embedded IMU and two cameras. Please note the cameras are not used for this work. We used logs from a bus and a truck with similar sensor housings for our experiments.

Now we describe the necessary notation and reference frames used in our system. The vehicle base frame, B is located in the center of the rear axle of the vehicle. Sensor readings from lidars and IMUs are represented in their respective sensor frames as $L^{(k)}$, and $I^{(k)}$ respectively. Here, $k \in [F_L - \text{Top}, F_R - \text{Top}]$ denotes the location of the sensor in the vehicle corresponding to front-left-top and front-right-top respectively. The GNSS measurements are reported in a world fixed frame, W , and transformed to B frame by performing a calibration routine outside the scope of this work. The GNSS system also has an embedded IMU which is transformed to the base frame, B as well. In our discussions the transformation matrix is denoted as, $\mathbf{T} = \begin{bmatrix} \mathbf{R}_{3 \times 3} & \mathbf{t}_{3 \times 1} \\ \mathbf{0}^\top & 1 \end{bmatrix} \in \text{SE}(3)$ and $\mathbf{R}\mathbf{R}^\top = \mathbf{I}_{3 \times 3}$, since the rotation matrix is orthogonal.

B. Problem formulation

Our primary goal is to estimate the extrinsic calibration of multiple lidar sensors in base frame, B in real-time without the need of any fiducial markers. We only use the raw IMU

signals from $\mathbf{I}^{(k)}$ and B frame (from GNSS system) and use the known extrinsics $\mathbf{T}_{\mathbf{I}^{(k)}\mathbf{L}^{(k)}}$ from sensor supplier to estimate $\mathbf{T}_{\mathbf{BL}^{(k)}}$. Additionally, we estimate the IMU biases online to denoise the raw IMU signals which improves the calibration quality.

IV. METHODOLOGY

A. Initialization

The IMU measurements are in their corresponding sensor frame. For gravity alignment, we use the equations [19, Eq. 25, 26] to estimate roll and pitch and obtain $\mathbf{R}_{\mathbf{WB}}$ after collecting IMU data when the vehicle is static for a few seconds.

B. IMU sensor model

We have considered a 6-DoF (degree of freedom) IMU such that it has a 3-axis accelerometer and 3-axis gyroscope. The IMU sensor data in its corresponding sensor frame can be represented as,

$$\begin{bmatrix} \boldsymbol{\omega}_{\mathbf{I}_t} \\ \mathbf{a}_{\mathbf{I}_t} \end{bmatrix} = \begin{bmatrix} \hat{\boldsymbol{\omega}}_{\mathbf{I}_t} \\ \hat{\mathbf{a}}_{\mathbf{I}_t} - \mathbf{R}_{\mathbf{WI}_t}^T \mathbf{g}_\mathbf{W} \end{bmatrix} + \begin{bmatrix} \mathbf{b}_{\mathbf{I}_t}^\omega \\ \mathbf{b}_{\mathbf{I}_t}^a \end{bmatrix} + \begin{bmatrix} \mathbf{n}_{\mathbf{I}_t}^\omega \\ \mathbf{n}_{\mathbf{I}_t}^a \end{bmatrix}. \quad (1)$$

Here, $[\boldsymbol{\omega}_{\mathbf{I}_t} \in \mathbb{R}^{3 \times 1}, \mathbf{a}_{\mathbf{I}_t} \in \mathbb{R}^{3 \times 1}]$ represent the measured angular velocity and linear acceleration at timestamp t and $[\hat{\boldsymbol{\omega}}_{\mathbf{I}_t}, \hat{\mathbf{a}}_{\mathbf{I}_t}]$ represent the latent ideal angular velocity and linear acceleration respectively. $\mathbf{b}_{\mathbf{I}_t}^\omega \in \mathbb{R}^{3 \times 1}$ and $\mathbf{b}_{\mathbf{I}_t}^a \in \mathbb{R}^{3 \times 1}$ represent the gyro and accelerometer biases which change with time and other factors like temperature. $\mathbf{n}_{\mathbf{I}_t}^\omega \sim \mathcal{N}(0, \boldsymbol{\Sigma}_\omega)$ and $\mathbf{n}_{\mathbf{I}_t}^a \sim \mathcal{N}(0, \boldsymbol{\Sigma}_a)$ are the additive zero-mean white Gaussian noises for gyroscope and accelerometer with covariance $\boldsymbol{\Sigma}_\omega \in \mathbb{R}^{3 \times 3}$ and $\boldsymbol{\Sigma}_a \in \mathbb{R}^{3 \times 3}$ respectively. $\mathbf{g}_\mathbf{W} \in \mathbb{R}^{3 \times 1}$, represents the gravity vector in W frame and $\mathbf{R}_{\mathbf{BW}}$ represent the gravity alignment rotation matrix.

C. IMU bias characterization

In our method, since we are not using an external odometry source for bias compensation we collect the data sequences with periods of rest in between. This limits the bias covariance growth as they converge faster after rest detection.

1) *IMU state propagation*: The IMU dynamical model based on angular velocity in quaternion form is shown as,

$$\mathbf{q}_{\mathbf{BI}_t} = \left[\cos\left(\frac{\Delta t}{2} \|\boldsymbol{\omega}_{\mathbf{I}_t}\|\right) \mathbf{I}_4 + \frac{\sin\left(\frac{\Delta t}{2} \|\boldsymbol{\omega}_{\mathbf{I}_t}\|\right)}{\|\boldsymbol{\omega}_{\mathbf{I}_t}\|} \boldsymbol{\Omega}_{\mathbf{I}_t} \right] \mathbf{q}_{\mathbf{BI}_{t-1}} \quad (2)$$

and,

$$\boldsymbol{\Omega}_{\mathbf{I}_t} = \begin{bmatrix} 0 & [\boldsymbol{\omega}_{\mathbf{I}_t}]_z & -[\boldsymbol{\omega}_{\mathbf{I}_t}]_y & [\boldsymbol{\omega}_{\mathbf{I}_t}]_x \\ -[\boldsymbol{\omega}_{\mathbf{I}_t}]_z & 0 & [\boldsymbol{\omega}_{\mathbf{I}_t}]_x & [\boldsymbol{\omega}_{\mathbf{I}_t}]_y \\ [\boldsymbol{\omega}_{\mathbf{I}_t}]_y & -[\boldsymbol{\omega}_{\mathbf{I}_t}]_x & 0 & [\boldsymbol{\omega}_{\mathbf{I}_t}]_z \\ -[\boldsymbol{\omega}_{\mathbf{I}_t}]_x & -[\boldsymbol{\omega}_{\mathbf{I}_t}]_y & -[\boldsymbol{\omega}_{\mathbf{I}_t}]_z & 0 \end{bmatrix}. \quad (3)$$

Δt denotes the sampling period of the IMU data. We used the Madgwick filter [20] to estimate the refined rotation which minimizes the difference between the measured acceleration and the aligned gravity vector using a gradient descent algorithm as,

$$\mathbf{q}_{\mathbf{BI}_t}^* = \arg \min_{\mathbf{q}_{\mathbf{BI}_t} \in \mathbb{R}^{4 \times 1}} \left(\tilde{\mathbf{q}}_{\mathbf{BI}_t} \otimes \mathbf{R}_{\mathbf{BW}}^{-1} \mathbf{g}_\mathbf{W} \otimes \mathbf{q}_{\mathbf{BI}_t} - \hat{\mathbf{a}}_{\mathbf{BI}_t} \right), \quad (4)$$

where, $\tilde{\mathbf{q}}$ represents the quaternion conjugate and \otimes is the quaternion product operator. Note that we use the compensated accelerometer signals after bias compensation which is discussed in IV-C.3.

2) *Rest detection*: Rest is detected if the difference between the norm of the aligned gravity vector and the acceleration vector is less than a predefined threshold, τ for at least more than 2 seconds. Thus,

$$\text{Rest detected} = \|\tilde{\mathbf{q}}_{\mathbf{BI}_t} \otimes \mathbf{g}_\mathbf{B} \otimes \mathbf{q}_{\mathbf{BI}_t}^* - \hat{\mathbf{a}}_{\mathbf{BI}_t}\|_2 \leq \tau \quad (5)$$

3) *Accelerometer bias estimation*: The accelerometer bias is estimated by computing the mean of the signal when stationary and the standard deviation gives us the co-variance of the white Gaussian noise. We recompute these parameters whenever the vehicle is stationary and keep it unchanged until the next rest period. If the rest period duration is N seconds then,

$$\begin{aligned} \mathbf{b}^a &= \frac{\Delta t}{N} \sum_{i=1}^N (\mathbf{a}_{\mathbf{I}_i} - \mathbf{R}_{\mathbf{BI}_i}^* \mathbf{R}_{\mathbf{BW}}^{-1} \mathbf{g}_\mathbf{W}), \\ \boldsymbol{\Sigma}_a &= \text{diag} \left(\frac{\Delta t}{N} \sum_{i=1}^N |\mathbf{a}_{\mathbf{I}_i} - \mathbf{b}^a|^2 \right), \\ \implies \hat{\mathbf{a}}_{\mathbf{I}_t} &= \mathbf{a}_{\mathbf{I}_t} + \mathbf{R}_{\mathbf{BI}_t}^* \mathbf{R}_{\mathbf{BW}}^{-1} \mathbf{g}_\mathbf{W} - \mathbf{b}^a - \mathcal{N}(0, \boldsymbol{\Sigma}_a). \end{aligned} \quad (6)$$

4) *Gyro bias estimation*: The initialization of the gyro bias is done in a similar fashion as we did for the accelerometer and recomputed whenever the rest period is detected. Thus,

$$\begin{aligned} \text{System State, } \hat{\mathbf{x}}_0 &= \mathbf{b}_{\mathbf{I}_0}^\omega = \frac{\Delta t}{N} \sum_{i=1}^N (\boldsymbol{\omega}_{\mathbf{I}_i}) \\ \text{Measurement Noise, } \mathbf{W}_0 &= \mathcal{N}(0, \boldsymbol{\Sigma}_\omega) \\ \text{Process Noise, } \mathbf{Q} &= (0.1^\circ/\text{sec})^2 \mathbf{I}_{3 \times 3} \\ \text{Initial Covariance, } \mathbf{P}_0 &= (0.3^\circ/\text{sec})^2 \mathbf{I}_{3 \times 3}. \end{aligned} \quad (7)$$

After that we use a Kalman filter [21] to track the gyroscope bias as a state. The system is modeled by,

$$\begin{aligned} \mathbf{x}_t &= \hat{\mathbf{x}}_{t-1} + \mathcal{N}(0, \mathbf{Q}) \\ \mathbf{y}_t &= \mathbf{R}_{\mathbf{BI}_t}^* \mathbf{x}_t + \mathbf{W}_t. \end{aligned} \quad (8)$$

The standard Kalman filter update equations become,

$$\begin{aligned} \mathbf{P}_t &= \mathbf{P}_{t-1} + \mathbf{Q} \\ \mathbf{K}_t &= \mathbf{P}_t \mathbf{R}_{\mathbf{BI}_t}^{*T} (\boldsymbol{\Sigma}_\omega + \mathbf{R}_{\mathbf{WI}_t}^* \mathbf{P}_t \mathbf{R}_{\mathbf{BI}_t}^{*T})^{-1} \\ \hat{\mathbf{x}}_t &= \hat{\mathbf{x}}_{t-1} + \mathbf{K}_t (\mathbf{y}_t - \mathbf{R}_{\mathbf{BI}_t}^* \hat{\mathbf{x}}_{t-1}) \\ \mathbf{P}_t &= \mathbf{P}_t - \mathbf{K}_t \mathbf{R}_{\mathbf{BI}_t}^* \mathbf{P}_t. \end{aligned} \quad (9)$$

Thus after estimating the biases we can rearrange eq. 1 to compute $\hat{\boldsymbol{\omega}}_{\mathbf{I}_t}$.

D. IMU-based lidar calibration

1) *Rotation estimation*: The extrinsics of $\mathbf{L}^{(k)}$ wrt B frame has a strong correlation with the extrinsics of $\mathbf{I}^{(k)}$ wrt B frame as they are collocated with known extrinsics from sensor supplier. A rigid body has the same angular velocity at all places. The angular velocities of all the IMU sensors in our sensor arrangement must be equal if their orientations

are the same because they are all securely affixed to the vehicle. Let, $[\hat{\omega}_{I_i^{(k)}}, \hat{\mathbf{a}}_{I_i^{(k)}}]$ and $[\hat{\omega}_{B_i}, \hat{\mathbf{a}}_{B_i}]$ be the estimated angular velocity and linear acceleration of the k^{th} IMU and the base IMU at timestamp t_i after bias compensation. By removing the k^{th} superscript for brevity, our optimization problem becomes,

$$\mathbf{R}_{BI}^* = \arg \min_{\mathbf{R}_{BI}} \sum_{i=1}^N \|\mathbf{R}_{BI} \hat{\omega}_{B_i} - \hat{\omega}_{I_i}\|_{\Sigma_i}^2, \quad (10)$$

$$s.t. \quad \mathbf{R}_{BI} \mathbf{R}_{BI}^T = \mathbf{I}_3,$$

which, can be simply solved with Horn alignment [22] or Kabsch alignment [23].

2) *Translation estimation:* For the acceleration components we compensate for the Coriolis forces as illustrated in Fig. 3 and equate the translation components as,

$$(\mathbf{R}_{BI}^*)^{-1} \hat{\mathbf{a}}_I = \hat{\mathbf{a}}_B + \underbrace{\hat{\omega}_B \times (\hat{\omega}_B \times \mathbf{t}_{BI})}_{\text{Centrifugal force}} + \underbrace{\dot{\hat{\omega}}_B \times \mathbf{t}_{BI}}_{\text{Euler force}} \quad (11)$$

$$= \hat{\mathbf{a}}_B + [\hat{\omega}_B]_{\times}^2 \mathbf{t}_{BI} + [\dot{\hat{\omega}}_B]_{\times} \mathbf{t}_{BI},$$

where, $[\cdot]_{\times}$ is a skew-symmetric matrix and $[\mathbf{a}]_{\times} \mathbf{b} = \mathbf{a} \times \mathbf{b}$.

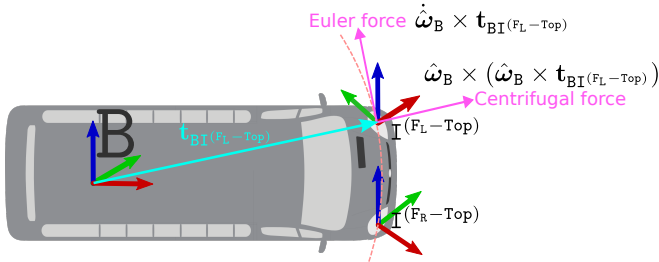


Fig. 3: Illustration of IMU signal transformation between B and $I^{(FL-Top)}$ frame.

Since, we already computed \mathbf{R}_{BI}^* , our optimization problem for the translation component becomes,

$$\mathbf{t}_{BI}^* = \arg \min_{\mathbf{t}_{BI}} \sum_{i=1}^N \underbrace{\|([\hat{\omega}_{B_i}]_{\times}^2 + [\dot{\hat{\omega}}_{B_i}]_{\times}) \mathbf{t}_{BI} - (\mathbf{R}_{BI}^{-1*} \hat{\mathbf{a}}_{I_i} - \hat{\mathbf{a}}_{B_i})\|_{\Sigma_i}^2}_{\mathbf{A}_i}, \quad (12)$$

where, $\mathbf{A} = [\mathbf{A}_0 \ \mathbf{A}_1 \ \dots \ \mathbf{A}_N]^T$, $\mathbf{B} = [\mathbf{B}_0 \ \mathbf{B}_1 \ \dots \ \mathbf{B}_N]^T$ and $\mathbf{x} = \mathbf{t}_{BI} \ \forall i \in [1, N]$. This is a system of linear equations of the form, $\mathbf{A}\mathbf{x} = \mathbf{B}$, which can be solved using a least-square approach as,

$$\mathbf{x}^* = \arg \min_{\mathbf{x}} \|\mathbf{A}\mathbf{x} - \mathbf{B}\|_{\Sigma}^2, \quad (13)$$

where, Σ denotes the co-variance of the residual. The main approach [24] used to tackle these problems involves solving a series of approximations to the original problem repeatedly by linearizing as, $F(\mathbf{x} + \Delta\mathbf{x}) \approx F(\mathbf{x}) + \mathbf{J}(\mathbf{x})\Delta\mathbf{x}$, where, \mathbf{J} being the jacobian of $F(\mathbf{x})$. Thus, $\hat{\mathbf{x}}$ is updated in the current iteration as, $\hat{\mathbf{x}} \leftarrow \hat{\mathbf{x}} \boxplus \Delta\mathbf{x}$, where \boxplus is an addition operator in the manifold and the problem becomes,

$$\Delta\mathbf{x}^* = \arg \min_{\Delta\mathbf{x}} \frac{1}{2} \|(\mathbf{A}\hat{\mathbf{x}} - \mathbf{B}) + \mathbf{A}^T \Delta\mathbf{x}\|_{\Sigma}^2. \quad (14)$$

The optimal solution is given by,

$$\underbrace{(\mathbf{J}^T \Sigma^{-1} \mathbf{J})}_{\text{Fisher information matrix}} \Delta\mathbf{x} = -\mathbf{J}^T \Sigma^{-1} (\mathbf{A}\hat{\mathbf{x}} - \mathbf{B}). \quad (15)$$

In practice, since we receive reliable initial estimate for the translation component from the CAD parameters, we search for \mathbf{x}^* only in a local neighborhood within reasonable bounds. Thus, we solve a bounded variable least squares problem as,

$$\mathbf{x}^* = \arg \min_{\mathbf{L} \leq \mathbf{x} \leq \mathbf{U}} \|\mathbf{A}\mathbf{x} - \mathbf{B}\|_{\Sigma}^2, \quad (16)$$

where, \mathbf{L} and \mathbf{U} are the lower and upper bounds of \mathbf{x} respectively. Thus the solution space in Eq. 14 is modified with an additional constraint as,

$$\Delta\mathbf{x}^* = \arg \min_{\Delta\mathbf{x}} \frac{1}{2} \|(\mathbf{A}\hat{\mathbf{x}} - \mathbf{B}) + \mathbf{A}^T \Delta\mathbf{x}\|_{\Sigma}^2, \quad (17)$$

$$s.t. \quad \mathbf{L} \leq \hat{\mathbf{x}} + \Delta\mathbf{x} \leq \mathbf{U}.$$

E. Observability analysis

All motions do not excite enough degrees of freedom to allow calibration. As a result, it's important to identify the motion segments for information-aware calibration updates. We capture this information by comparing the angular velocity between $I^{(k)}$ and B frame based on Eq.10 which can also be solved iteratively with the update step as,

$$\underbrace{\left(\sum_i \mathbf{J}_i^T \Sigma_i^{-1} \mathbf{J}_i \right)}_{\text{Fisher information matrix}} \Delta\mathbf{R}_{BI} \stackrel{\text{Eq. 15}}{=} - \sum_i \mathbf{J}_i^T \Sigma_i^{-1} (\hat{\mathbf{R}}_{BI} \hat{\omega}_{B_i} - \omega_{I_i}) \quad (18)$$

where, $\Sigma_i = \text{cov}(\hat{\mathbf{R}}_{BI} \hat{\omega}_{B_i} - \omega_{I_i})$ and $\mathbf{J}_i = \omega_{B_i}^T$. The Fisher information matrix, $\mathcal{I}_{N \times N}$ captures all the information contained in the measurements. We do the processing after arranging the data in a batch size of N . We perform a Singular Value Decomposition of $\mathcal{I}_{N \times N}$ for each batch as:

$$\mathcal{I}_{N \times N} = \mathbf{U} \mathbf{S} \mathbf{U}^T, \quad (19)$$

where, $\mathbf{U} = [\mathbf{u}_1, \mathbf{u}_2, \dots, \mathbf{u}_N]$ and $\mathbf{S} = \text{diag}(\sigma_1, \sigma_2, \dots, \sigma_N)$ is a diagonal matrix of singular values in decreasing order. Information about the data in the batch is indicated by the value of the minimal singular value. If the minimal singular value exceeds a certain threshold (design decision), we may say that there are sufficient excitations in the batch of data to allow for extrinsics computation and hence chosen for calibration.

V. EXPERIMENTAL RESULTS

To demonstrate the online calibration performance, we conducted several experiments with real-world data collected using two vehicles with the sensor setup illustrated in Fig. 2.

A. Dataset

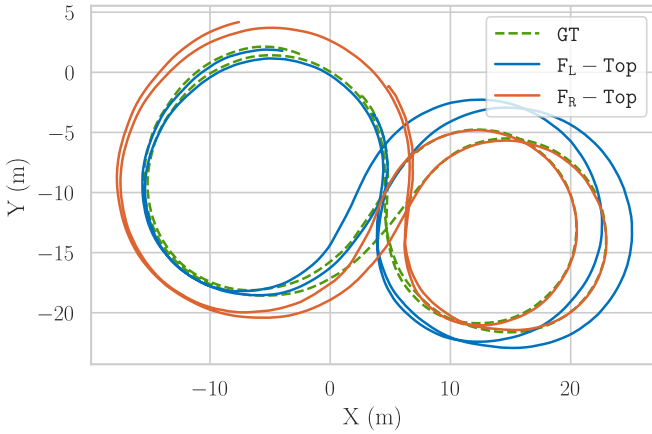
We use data from a GNSS receiver for the GT (ground truth) poses. We analyze our results on 2 different collected test sequences which are described in detail in Table I, covering different driving scenarios. In Seq-1, we performed aggressive motion to excite the possible degrees of freedom.

However, in Seq-2 we recorded data in a normal driving scenario in regular traffic conditions. In Seq-1, there were no periods of rest whereas in Seq-2 there were occasional periods of rest due to traffic signals.

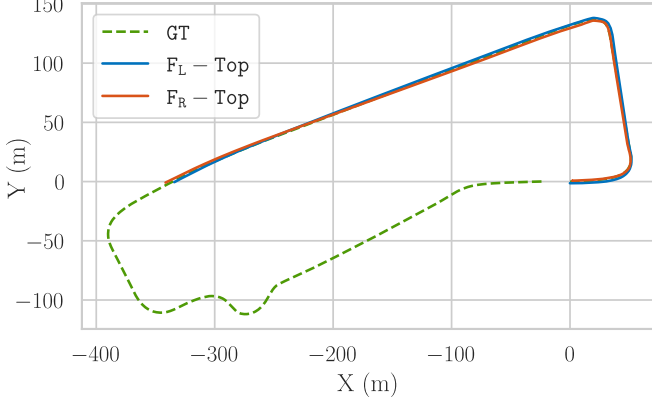
| Dataset collection details for the experiments | | | | |
|--|---------|-------------|-----------------|-------------|
| Data | Vehicle | Length (Km) | Duration (secs) | Stop period |
| Seq-1 [†] | Truck | 0.224 | 81 | No |
| Seq-2 [†] | Bus | 1.088 | 283 | Yes |

[†]F_L – Top, F_R – Top mounted lidars were used for the experiments.

TABLE I



(a) Seq-1: Odometry estimation in aggressive driving scenario.



(b) Seq-2: Odometry estimation in non-aggressive driving scenario.

Fig. 4: Odometry estimation of F_L – Top and F_R – Top lidars using Fast-lio2 [25] for both the sequences. The trajectory alignment is done using Kabsch alignment [23].

We evaluated the performance of a state-of-the-art lidar odometry estimator (Fast-lio2 [25]) on both the motion sequences as seen in Fig. 4 and observe that the estimator is sensitive to the aggressive motion sequence, Seq-1. The RMSE of the absolute pose error (APE) for Seq-1 is 2.2926m and 2.1063m for F_L – Top and F_R – Top lidars respectively, which is not suitable for motion-based calibration using pose alignment strategies. As seen in Fig. 4a, the Kabsch alignment [23] algorithm does not lead us to correct trajectory alignment. For Seq-2, the APE is less than 0.5 m for both lidars when

using Fast-lio2. However, this motion sequence doesn't have enough excitation in all the different degrees of freedom and thus is not a great choice for a calibration motion sequence using our proposed method. We did not run the state estimator for the whole sequence as not enough excitation for the different degrees of freedom was present in the data.

B. Bias estimation results

To improve our calibration performance, which relies on the signal-to-signal match policy we compensate for the biases in both the accelerometer and angular velocity signals. The accelerometer biases are recomputed whenever a period of rest is detected. The angular velocity biases are tracked online based on the Kalman filter. The update step is based on the estimated orientation using the Madgwick filter that uses the bias-compensated accelerometer signals for gravity alignment. Thus whenever a period of rest is detected the covariances of the angular velocity biases converge.

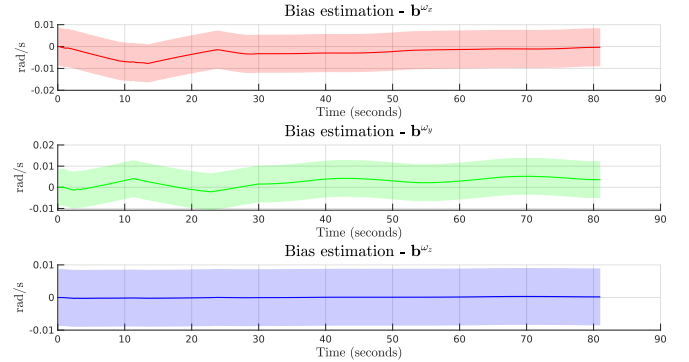


Fig. 5: Bias estimation for the F_L – Top angular velocity signals for Seq-1.

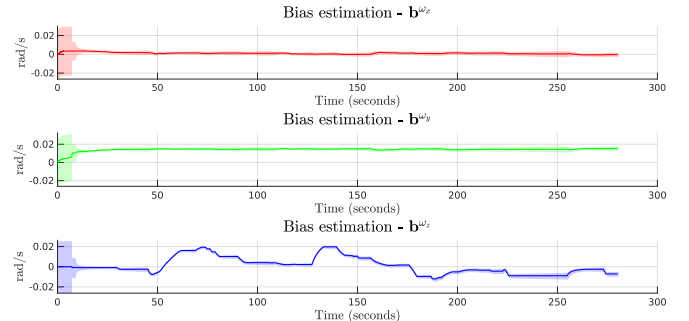


Fig. 6: Bias estimation for the F_L – Top angular velocity signals for Seq-2.

In Seq-1, we didn't have any periods of rest. Thus the angular velocity bias covariances do not converge as seen in Fig. 5. Whereas, in Fig. 6, we see that the angular velocity bias covariances converge after the detection of the rest period for a few seconds at the beginning of Seq-2.

C. Online calibration results

GT calibration of the lidars is obtained offline by refining the vehicle CAD parameters. The refinement process analyzes

known static feature positions around the vehicle in the world frame, \mathbf{W} , and matches the corresponding detected features from the lidar perspective. After that, we obtain the extrinsics of the lidars to the base frame, \mathbf{B} and compute the transformation matrix, $\mathbf{T}_{\text{GT}} = \mathbf{T}_{\text{BL}(\text{F}_L - \text{Top})}^{-1} \mathbf{T}_{\text{BL}(\text{F}_R - \text{Top})}$, between the 2 lidars. We compare our results to this matrix by comparing the translation and rotation errors as:

$$\Delta t = \frac{1}{3} \sqrt{\|\hat{\mathbf{t}} - \mathbf{t}_{\text{GT}}\|_F^2}, \quad (20)$$

$$\Delta R = \frac{180}{\pi} \cos^{-1} \left[\frac{1}{2} \left(\text{Tr}(\hat{\mathbf{R}}^{-1} \mathbf{R}_{\text{GT}}) - 1 \right) \right], \quad (21)$$

where, ΔR is the rotation along the principle eigenvector of $(\hat{\mathbf{R}}^{-1} \mathbf{R}_{\text{GT}})$.

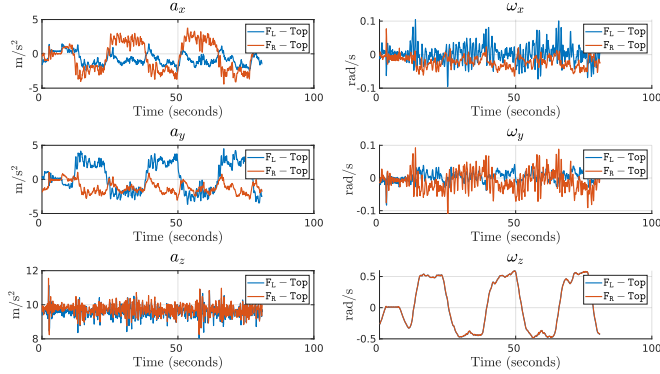


Fig. 7: Raw IMU signals from $\text{F}_L - \text{Top}$ and $\text{F}_R - \text{Top}$ IMUs for Seq-1.

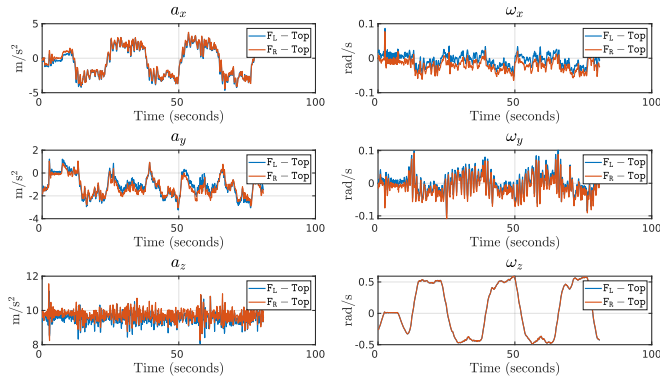


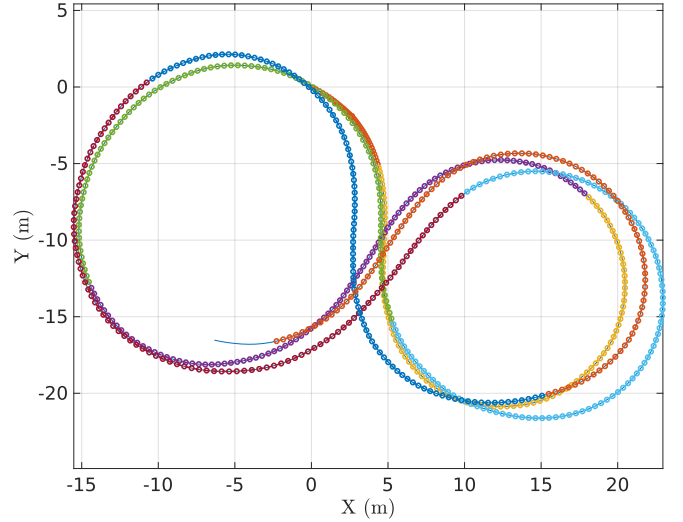
Fig. 8: Calibrated IMU signals from $\text{F}_L - \text{Top}$ and $\text{F}_R - \text{Top}$ IMUs with bias compensation for Seq-1.

For Seq-1, we obtained $\Delta t = 0.3387\text{m}$ and $\Delta R = 0.4577^\circ$ and the original IMU signals, as well as the calibrated IMU signals between the 2 collocated IMUs, can be observed in Fig. 7 and Fig. 8 respectively. For Seq-2, the results were, $\Delta t = 0.4431\text{m}$ and $\Delta R = 4.7938^\circ$. For both the sequences, the translation components were obtained by solving a bound variable least square optimization problem as defined in Eq.16 with bounds of $\pm 0.3\text{m}$. The raw and calibrated signals for Seq-2 are additionally shown in our complimentary video. As expected, in Seq-1, due to the presence of rich motion sequence in terms of excitation of different degrees of freedom

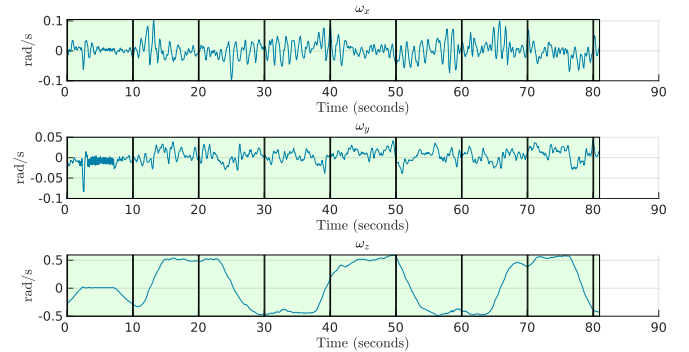
our signal matching algorithm produces better results than Seq-2.

D. Observability analysis

For observability analysis we extract the information matrix by comparing the angular velocity signals between the collocated IMU, $\mathbf{I}^{(k)}$, and the B frame by dividing the data into equal segments of 10 sec each. We analyze the SVD of the Fisher information matrix from Eq.18 and select the IMU data in the segment for calibration if the minimum singular value is greater than a threshold. For our experiments, we set the threshold as 5^{-10} .



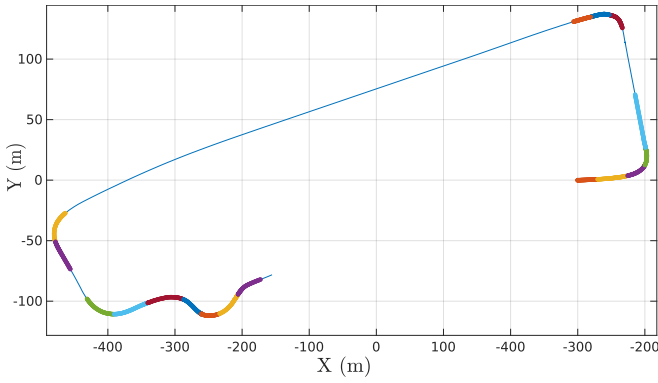
(a) Selected poses with observability criteria for Seq-1 shown with random colors.



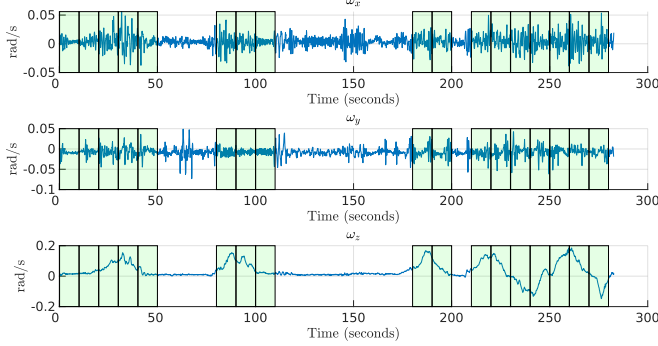
(b) The angular velocity signals in different motion segments in a 10 sec window.

Fig. 9: Seq-1: The observability criteria selects all the motion segments as there were enough excitation in the angular velocity signals in all the motion segments.

As seen in Fig. 9b, we selected all segments (highlighted in green) as there was enough excitation in the angular velocity during all the time in Seq-1. The corresponding selected trajectory segments are shown in Fig. 9a. Similarly for Seq-2, we can see that in Fig. 10a, relevant poses for calibration are selected only when there are significant turns in the maneuvers as observed in Fig. 10b, meaning there is enough excitation for different degrees of freedom.



(a) Selected poses with observability criteria for Seq-2 shown with random colors.



(b) We observe that in straight motion segments there are not enough excitation in the angular velocity for Seq-2. Hence, the straight motion segments are not used from observability perspective and thus ignored for calibration.

Fig. 10: Seq-2: The observability criteria selects motion segments when there were enough excitation in the angular velocity signals, particularly during the turns.

VI. CONCLUSION

We show that it is possible to estimate the extrinsic calibration of multiple lidars based on matching collocated IMU signals only. Unlike other methods which use odometry estimates for matching poses, this is a lightweight method that relies on raw signal matching. The observability-aware module selects signals that carry enough excitation for different degrees of freedom required for calibration. Our method provides comparable performance to GT extrinsics parameters when sufficient signal excitations are present. This work can be easily extended to other modalities like cameras and radars. For further improvement, we can also match features in between the corresponding sensors if they have a common FoV.

VII. ACKNOWLEDGEMENTS

This research has been jointly funded by the Swedish Foundation for Strategic Research (SSF) and Scania. The research was also affiliated with Wallenberg AI, Autonomous Systems and Software Program (WASP).

REFERENCES

[1] M. He, H. Zhao, F. Davoine, J. Cui, and H. Zha, "Pairwise lidar calibration using multi-type 3d geometric features in natural scene," in *IEEE International Conference on Intelligent Robots and Systems*, 2013, pp. 1828–1835.

[2] D.-G. Choi, Y. Bok, J.-S. Kim, and I. S. Kweon, "Extrinsic calibration of 2-d lidars using two orthogonal planes," *IEEE Transactions on Robotics*, vol. 32, no. 1, pp. 83–98, 2016.

[3] J. Brookshire and S. Teller, "Extrinsic calibration from per-sensor egomotion," *Robotics: Science and Systems VIII*, pp. 504–512, 2013.

[4] L. Heng, B. Li, and M. Pollefeys, "Camodocal: Automatic intrinsic and extrinsic calibration of a rig with multiple generic cameras and odometry," in *IEEE International Conference on Intelligent Robots and Systems*. IEEE, 2013, pp. 1793–1800.

[5] P. Furgale, J. Rehder, and R. Siegwart, "Unified temporal and spatial calibration for multi-sensor systems," in *IEEE International Conference on Intelligent Robots and Systems*, 2013, pp. 1280–1286.

[6] J. Jiao, H. Ye, Y. Zhu, and M. Liu, "Robust odometry and mapping for multi-lidar systems with online extrinsic calibration," *IEEE Transactions on Robotics*, vol. 38, no. 1, pp. 351–371, 2021.

[7] J. Lv, X. Zuo, K. Hu, J. Xu, G. Huang, and Y. Liu, "Observability-aware intrinsic and extrinsic calibration of lidar-imu systems," *IEEE Transactions on Robotics*, 2022.

[8] J. Maye, P. Furgale, and R. Siegwart, "Self-supervised calibration for robotic systems," in *IEEE Intelligent Vehicles Symposium*, 2013, pp. 473–480.

[9] K. Hausman, J. Preiss, G. S. Sukhatme, and S. Weiss, "Observability-aware trajectory optimization for self-calibration with application to uavs," *IEEE Robotics and Automation Letters*, vol. 2, no. 3, pp. 1770–1777, 2017.

[10] T. Schneider, M. Li, C. Cadena, J. Nieto, and R. Siegwart, "Observability-aware self-calibration of visual and inertial sensors for ego-motion estimation," *IEEE Sensors Journal*, vol. 19, no. 10, pp. 3846–3860, 2019.

[11] R. Tsai and R. Lenz, "A new technique for fully autonomous and efficient 3d robotics hand/eye calibration," *IEEE Transactions on Robotics and Automation*, vol. 5, no. 3, pp. 345–358, 1989.

[12] R. Horaud and F. Dornaika, "Hand-eye calibration," *The international journal of robotics research*, vol. 14, no. 3, pp. 195–210, 1995.

[13] J. Jiao, Y. Yu, Q. Liao, H. Ye, R. Fan, and M. Liu, "Automatic calibration of multiple 3d lidars in urban environments," in *IEEE International Conference on Intelligent Robots and Systems*, 2019, pp. 15–20.

[14] S. Das, N. Mahabadi, A. Djikic, C. Nassir, S. Chatterjee, and M. Fallon, "Extrinsic calibration and verification of multiple non-overlapping field of view lidar sensors," in *IEEE International Conference on Robotics and Automation*, 2022, pp. 919–925.

[15] J. Rehder, J. Nikolic, T. Schneider, T. Hinzmann, and R. Siegwart, "Extending kalibr: Calibrating the extrinsics of multiple imus and of individual axes," in *IEEE International Conference on Robotics and Automation*. IEEE, 2016, pp. 4304–4311.

[16] K. Eickenhoff, P. Geneva, and G. Huang, "Mimc-vins: A versatile and resilient multi-imu multi-camera visual-inertial navigation system," *IEEE Transactions on Robotics*, vol. 37, no. 5, pp. 1360–1380, 2021.

[17] J.-O. Nilsson, I. Skog, and P. Händel, "Aligning the forces—eliminating the misalignments in imu arrays," *IEEE Transactions on Instrumentation and Measurement*, vol. 63, no. 10, pp. 2498–2500, 2014.

[18] M. E. Pittelkau, "Calibration and attitude determination with redundant inertial measurement units," *Journal of Guidance, Control, and Dynamics*, vol. 28, no. 4, pp. 743–752, 2005.

[19] M. Pedley, "Tilt sensing using a three-axis accelerometer," *Freescall semiconductor application note*, vol. 1, pp. 2012–2013, 2013.

[20] S. O. H. Madgwick, A. J. L. Harrison, and R. Vaidyanathan, "Estimation of imu and marg orientation using a gradient descent algorithm," in *2011 IEEE International Conference on Rehabilitation Robotics*, 2011, pp. 1–7.

[21] R. E. Kalman, "A new approach to linear filtering and prediction problems," *Transactions of the ASME—Journal of Basic Engineering*, vol. 82, no. Series D, pp. 35–45, 1960.

[22] B. K. Horn, "Closed-form solution of absolute orientation using unit quaternions," *Journal of the Optical Society of America*, vol. 4, no. 4, pp. 629–642, 1987.

[23] W. Kabsch, "A discussion of the solution for the best rotation to relate two sets of vectors," *Crystallographica: Crystal Physics, Diffraction, Theoretical and General Crystallography*, pp. 827–828, 1978.

[24] J. Nocedal and S. J. Wright, *Numerical optimization*. Springer, 1999.

[25] W. Xu, Y. Cai, D. He, J. Lin, and F. Zhang, "FAST-LIO2: Fast direct lidar-inertial odometry," *IEEE Transactions on Robotics*, vol. 38, no. 4, pp. 2053–2073, 2022.